Solar light-activated photocatalytic degradation of gas phase diethylsulfide on WO₃-modified TiO₂ nanotubes

Mathieu Grandcolas [a], Thomas Cottineau [a], Alain Louvet [b], Nicolas Keller [a], Valérie Keller [a,*]

[a] Institut de Chimie et Procédés pour l'Energie, l'Environnement et la Santé (ICPEES), CNRS, University of Strasbourg, 25 rue Becquerel 67087, Strasbourg, France
[b] Direction Générale de L'Armement (DGA), DGA CBRN Defense, BP 3, 91710 Vert-le-Petit, France

ARTICLE INFO

ABSTRACT

Artificial solar light responsive high surface area WO₃-modified TiO₂ nanotubes have been efficiently used for performing the gas phase photocatalytic degradation of diethylsulfide, taken as simulant for the live yperite Chemical Warfare blister Agent, known as mustard gas. They were prepared by impregnating hydrothermally-synthesized titanate nanotubes with tungstate salt prior to the final calcination step. The influence of the WO₃ content, the inlet diethylsulfide concentration and the relative humidity on the photocatalytic activity as a function of time on stream has been investigated in terms of DES removal efficiency and of deactivation behavior. Modification of TiO₂ nanotubes with 4 wt.% of WO₃ enhanced the photocatalytic activity in terms of DES removal efficiency and of resistance to sulfate deactivation. Correlation between the surface species and the on-stream activity and behavior of the photocatalysts was proposed, as well as possible reaction mechanism pathways.

© 2013 Elsevier B.V. All rights reserved.

1. Introduction

Recent years have seen the emergence of numerous techniques which are of high interest for environmental applications, particularly for treating chemically- and biologically-contaminated water, air and substrates. Among them, photocatalysis offers significant opportunities in various areas [1], partly taking advantage from recent advances in the field of nanomaterials and in that of photochemical engineering. Embedded into filtration systems, paints, coatings and other so-called functional materials, photocatalysis seems to establish itself as an innovative technique and to be part of technological advances gained in logic of sustainable development.

The risk of hazardous chemical dispersion has become a growing threat, increasing strongly the potential risks of exposure to toxic materials. It is thus necessary to consider materials and protection systems for suitable decontamination. Dispersion of toxic agents results in both equipment and infrastructure contamination, so that one should focus on ways that allow decontamination and reduce the risk of dispersion. Nowadays, most decontamination systems are resources-, time- and logistics-consuming, and require large amounts of water, corrosives or toxics, so that they are not considered as environmentally friendly. There are currently decontamination systems that can degrade the targeted chemical

or biological agents. However, they must be implemented after the event and after first-responder intervention, so that, till the decontamination technology can operate, the risk remains with continuous hazards toward the contaminated people, the surrounding people and stakeholders.

Photocatalysis has already been successfully used for degrading organosulfur compounds such as diethylsulfide (DES), acting as a simulant for the live yperite Chemical Warfare Agent (CWA), blister agent also known as mustard gas [2–4], whereas it has also been scarcely directly applied on live blister yperite CWA [5–7]. One should also note the interesting investigations performed on the photocatalytic oxidation of nauseous organosulfides such as dimethylsulfides [8,9].

TiO₂ has been shown to be one of the best candidates for use as photocatalyst. Since the discovery of one-dimension nanocarbons like nanotubes or nanofibers, and within the trend to develop similar carbon-free high aspect ratio nanomaterials, titania-based nanotubes have started to attract much attention for use in various applications [10], like photovoltaic cells, gas sensors, UV blockers. They also targeted promising applications in photocatalysis or photo-electrocatalysis for environmental and renewable energy production technologies, and more generally for sustainable development applications, due to their unique behaviors resulting from their nanotubular structure [11–17]. The high aspect ratio structure offers a large surface-to-volume ratio resulting in a large surface area available and enhanced adsorption capacity for the reactant adsorption step. It also allows possible size confinement

* Corresponding author. Tel.: +33 368852736; fax: +33 368852761.
  E-mail address: vkeller@unistra.fr (V. Keller).

in radial-direction to take place and leads to electron transfer properties enhancement. The charge delocalization through the tubular shape consequently enhances the spatial charge separation of photogenerated electrons and holes and thus reduces the charge recombination rates [10,18–20].

A simple and cost-effective hydrothermal method for producing nanotubular titania materials was proposed by Kasuga et al. [21]. However, the band gap of titania-based nanotubes (and more generally that of conventional TiO_2 anatase) restricted the use of such materials to UV-A applications. Therefore, the development of solar or visible light responsive high aspect ratio titania-based nanotubes is also of interest for targeting solar light applications. Among many methods explored, and in parallel to its positive influence for improving the UV-A photocatalytic activity in liquid and gas phase oxidation reactions [22–26], the coupling of a smaller band gap semiconductor such as WO_3 to titania is also a promising route for extending absorption into the visible light range and targeting solar photocatalysis applications, due to a 2.8–3.0 eV band gap energy falling within the solar spectrum [25–29]. The association of WO_3 with high aspect ratio titania nanostructures has also been studied more recently. Cheng et al. have synthesized highly ordered 100 nm diameter WO_3/TiO_2 composite nanotubes by combining a sol-gel method and an anodic alumina templating method [30]. Anodization has also been used for preparing WO_3/TiO_2 composite nanotubes with enhanced electrochromic properties [31].

The aim of the paper is thus to report on the synthesis and use of WO_3-modified titania nanotubes for the artificial solar light photocatalytic removal of gas phase DES as simulant of the live yperite organosulfide CWA. The thermal regeneration of the photocatalyst is also studied. The role of WO_3 and of the WO_3–nanotube interface as well as the correlation between the surface species, the photocatalytic activity and the deactivation phenomena are investigated, so that reaction mechanism pathways are proposed.

2. Experimental

2.1. Photocatalyst preparation

Titanate nanotubes (TiNTs) were first synthesized by the hydrothermal concentrated alkaline treatment of a crystallized TiO_2 powder [18]. In a typical synthesis, 2 g of TiO_2 P25 from Degussa-Evonik was dispersed for 1 h under stirring in 100 mL of 10 M concentrated NaOH. The mixture was then hydrothermally treated in a Teflon autoclave for 24 h at 130 °C, and the white powder obtained was rinsed with deionized water and subsequently vacuum filtered (TiNT-Na). After further washing with 1 M HCl, the material was finally rinsed with distilled water until neutral pH and dried overnight at 110 °C (TiNT-H). The crude as-synthesized material was then impregnated with the desired amount of $(NH_4)_{10}W_{12}O_{41}, 5H_2O$ pentahydrated ammonium paratungstate (99.5%, Sigma–Aldrich) in an ethanol/deionized water solution (1/3) for 15 h, further dried at 110 °C for 2 h and finally calcined in air at 380 °C for 2 h (TiNT-WO_3 x wt.%). A sample calcined at 380 °C without ammonium salt impregnation has also been prepared for comparison (TiNT-380).

2.2. Characterization techniques

X-ray diffraction (XRD) measurements were carried out on a D8 Advance Bruker diffractometer, in a $\theta/2\theta$ mode and using the $K\alpha_1$ radiation of Cu at 1.5406 Å.

Scanning electron microscopy (SEM) was carried out on a Jeol JSM-6700F at 3 kV voltage, equipped with a CCD camera. Prior to analysis, the sample was coated with gold.

Surface area and porosimetry measurements were carried out on a ASAP2010 Micromeritics Tristar apparatus using N_2 as adsorbant at liquid N_2 temperature. Before N_2 adsorption, the material was outgassed at 200 °C for 1 h. The specific surface area was calculated from the N_2 adsorption isotherm using the BET method, the micropore surface area was derived using the t-plot method, and the pore size distribution was obtained using the BJH method during the desorption isotherm branch.

X-ray photoelectron spectroscopy (XPS) characterization was performed on a Multilab 2000 (Thermo) spectrometer equipped with Al $K\alpha$ anode ($h\nu$ = 1486.6 eV). The energy shift due to electrostatic charging was subtracted using the contamination carbon C 1s band at 284.6 eV. The spectra were decomposed assuming contributions with a Doniach–Sunjic shape [32] and a Shirley background subtraction [33]. Etching Ar$^+$ bombardment was performed at 2 kV and 18 mA of ionic current. Sulfur-to-titanium (S/Ti), sulfur-to-tungsten (S/W) and tungsten-to-oxygen (W/O) surface atomic ratios have been calculated using the sensitivity factors, as determined by Scofield [34].

Transmission electron microscopy (TEM) was performed on a Topcon 002B microscope working with a voltage of 200 kV and a point-to-point resolution of 0.17 nm. The sample was sonically dispersed in an ethanol solution before a drop of the solution was deposited onto a copper grid covered by a holey carbon membrane for observation.

UV–vis absorption spectra of the materials were recorded on a Varian Cary 100 Scan spectrophotometer equipped with a DRA-CA-301 *Labsphere* diffuse reflectance cell. Thermal gravimetry analysis (TGA) was performed using a Q 5000 (TA Instruments) thermoanalyser with a heating rate of 15 °C/min, using a 20% (v/v) O_2/N_2 mixture at a flow rate of 50 mL/min. Temperature programmed oxidation (TPO) coupled to mass spectrometry analysis was also performed with a heating rate of 15 °C/min, using a 10% (v/v) O_2/He mixture at a flow rate of 50 mL/min.

Infrared Fourier transform spectroscopy (IRTF) was carried out with a Nicolet 205X apparatus working in transmittance mode using a sample/KBr (10/90 wt.%) pellet.

IsoElectrical Point (IEP) measurements were performed on a Malvern© ZetaSizer with automatic titration.

2.3. Experimental device and procedure

Gas phase photocatalysis was carried out in a 300 mm length single pass annular Pyrex reactor made of two coaxial tubes 3 mm apart, between which the reactant mixture was passing through. Extensive details concerning both photocatalytic reactor and device can be found elsewhere [35]. 420 mg of photocatalytic material, corresponding to a reactor surface coverage of 1.77 mg/cm^2, was evenly coated on the internal side of the 32 mm diameter external tube by evaporating a catalyst-containing aqueous slurry to dryness. The catalyst coated reactor was finally dried at 110 °C for 1 h in air. DES (Aldrich, 98%) and water were fed at ambient temperature and atmospheric pressure by bubbling air through two saturators respectively, and mixed with additional air to obtain the required DES-water-air ratios with a constant total air flow. Standard test conditions were 350 ppmv of DES, 40% relative humidity (RH) and 50 cm^3/min total flow, but the DES content was ranged from 100 to 1000 ppmv (*i.e.* 0.4 to 4 g DES per m^3 of flowing air) and RH was ranged from 0% to 80%. 100% of relative humidity was defined as the saturated vapor pressure of water at 25 °C, which corresponds to about 24 Torr, *i.e.* about 3% relatively to the total atmospheric pressure. Before the reaction, the catalyst was first exposed to the reactant-containing air stream with no illumination until dark-adsorption equilibrium was reached. Afterwards the illumination was switched on. It was provided by a commercial 24 W solar light simulating lamp (Philips DeLuxe pro LTJHo)

located inside the inner tube of the reactor. The emission spectrum of the solar light-simulating lamp is given as SI1, with a total irradiance composed of 42.5 W/m^2 of visible light and of 0.7 W/m^2 of UV-A, representing a fraction of 1.6% of the total irradiance. Reactants and reaction products were analyzed *on-line* by an Agilent GC-6890 N Gas Chromatography equipped with HP Plot Q and HP-5MS columns, coupled to a thermal conductivity detector and a MS-5973N Mass Spectrometer, respectively.

Gas phase regeneration of the photocatalyst was conducted after a first DES degradation test by thermal treatment at 90 °C using a tubular furnace wrapping the reactor, in similar operating conditions that those of the DES degradation tests in terms of flow rate and relative humidity, so except the absence of DES flow.

3. Results and discussion

3.1. Material characterization

3.1.1. Structural and morphological characterizations

The WO$_3$ content in the TiNT-WO$_3$ samples was obtained by Atomic Absorption Spectroscopy performed at the Service Central d'Analyse of the CNRS in Vernaison (France). TiNT-WO$_3$ materials experimentally loaded with 2 wt.%, 4 wt.% and 8 wt.% of WO$_3$ displayed contents of 1.7 wt.%, 3.7 wt.% and 7.8 wt.% respectively. This close agreement validated the impregnation procedure used and led to further name the samples with their respective theoretically deposited WO$_3$ contents.

Fig. 1 shows the XRD patterns of TiNT-Na, TiNT-H and TiNT-WO$_3$ (4 wt.% and 8 wt.%) one-dimension nanostructures at different steps of the synthesis, and TEM analysis evidenced their morphology and microstructure in Figs. 2 and 3. Coupled to SEM analysis of Fig. 4, it was worth noting the total selectivity of the hydrothermal synthesis toward the high aspect ratio nanomaterial, with no nanopowder being observed in the sample. Fig. 2 shows the nanosheet structure of the as-synthesized TiNT-Na nanomaterial before acidic neutralization, with 30 nm mean thickness and several hundreds of nm length. The diffraction peaks confirmed the sodium titanate form of the nanosheets, of Na$_2$Ti$_3$O$_7$ type, with diffraction peaks at 30.2°, 34.4°, 35.5°, 38.1° and 41.6° [36–38]. After neutralization washing with HCl and drying at 110 °C, the interlayered partial or total cation exchange between Na$^+$ and H$^+$, considered as the driving force for bending and rolling up of the nanosheets, resulted in the transformation of nanosheets into nanotubes. The broad peak at low diffraction angles around 10° was characteristic of the interlayer distance of the lamellar material [39,40]. The nanotubes displayed lengths of several hundreds of nm and mean diameters of 10–20 nm. The Na$^+$ to H$^+$ substitution was confirmed by the diffraction peaks, observed at $2\theta = 24.3°$,
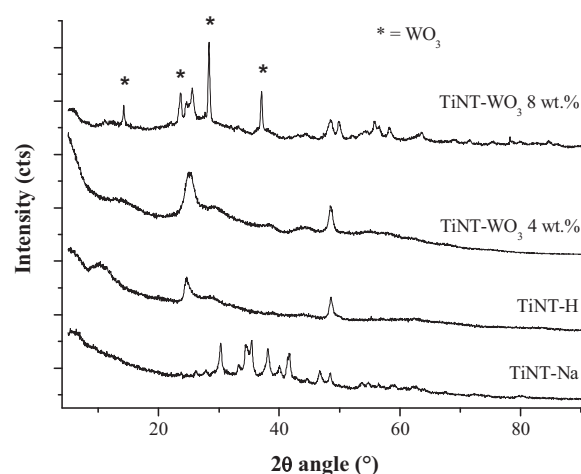

Fig. 1. XRD patterns of the crude titanates synthesized by the hydrothermal method (TiNT-Na), and further after washing with HCl until neutralization and drying (TiNT-H) and both TiNT-WO$_3$ (4 wt.%) and TiNT-WO$_3$ (8 wt.%) after impregnation and final calcination at 380 °C.

28.5° and 49.5° and indexed to the H$_2$Ti$_3$O$_7$-like titanate structure [41]. A partial interlayered cation exchange could lead to the intermediate Na$_x$H$_{2-x}$Ti$_3$O$_7$ nanotubes as reported by Sun et al. [41]. However, elementary analysis, XPS and the absence of any residual sodium detected by Electron Dispersive Spectroscopy (EDS) during TEM was in favor of a total cation exchange and of the obtention of H$_2$Ti$_3$O$_7$ nanotubes. Although those nanotubes have a different crystallographic structure from TiO$_2$ anatase, one should mention that the exact structure remained still under discussion [42], and different structures were proposed such as lepidocrocite H$_x$Ti$_{2-x/4}$□$_{x/4}$O$_4$ ($x \sim 0.7$, □: vacancy) [43] or Na$_2$Ti$_3$O$_7$ [44,45].

After impregnation with the paratungstate salt and the final calcination at 380 °C, the XRD pattern exhibited diffraction peaks corresponding to the TiO$_2$(B) structure, with the main peaks at 24.4 and 48.5° corresponding to B(1 1 0) and B(0 2 0) planes, respectively [46,47]. Even if these peaks are very close to those of anatase TiO$_2$ – with main diffraction peaks at 24.8° and 48.3° corresponding to (1 1 0) and (0 2 0) planes [48] –, the discrimination could be confirmed looking at the broad peak at 29.6°, exclusively assigned to B(1 1 1) planes.

In addition, the footprint at low diffraction angles of the layered structure disappeared in favor of a broad diffraction peak around 14.3°, assigned to non-resolved TiO$_2$(B) crystal planes, and resulting also from an increase in the wall thickness due to a slight contraction of the nanotubes and thus of the crystallographic cell, caused by the inter-wall intrinsic dehydration of the nanotubes during
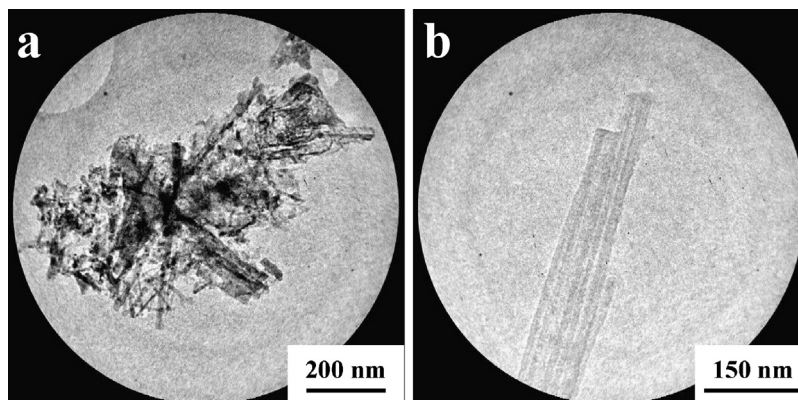

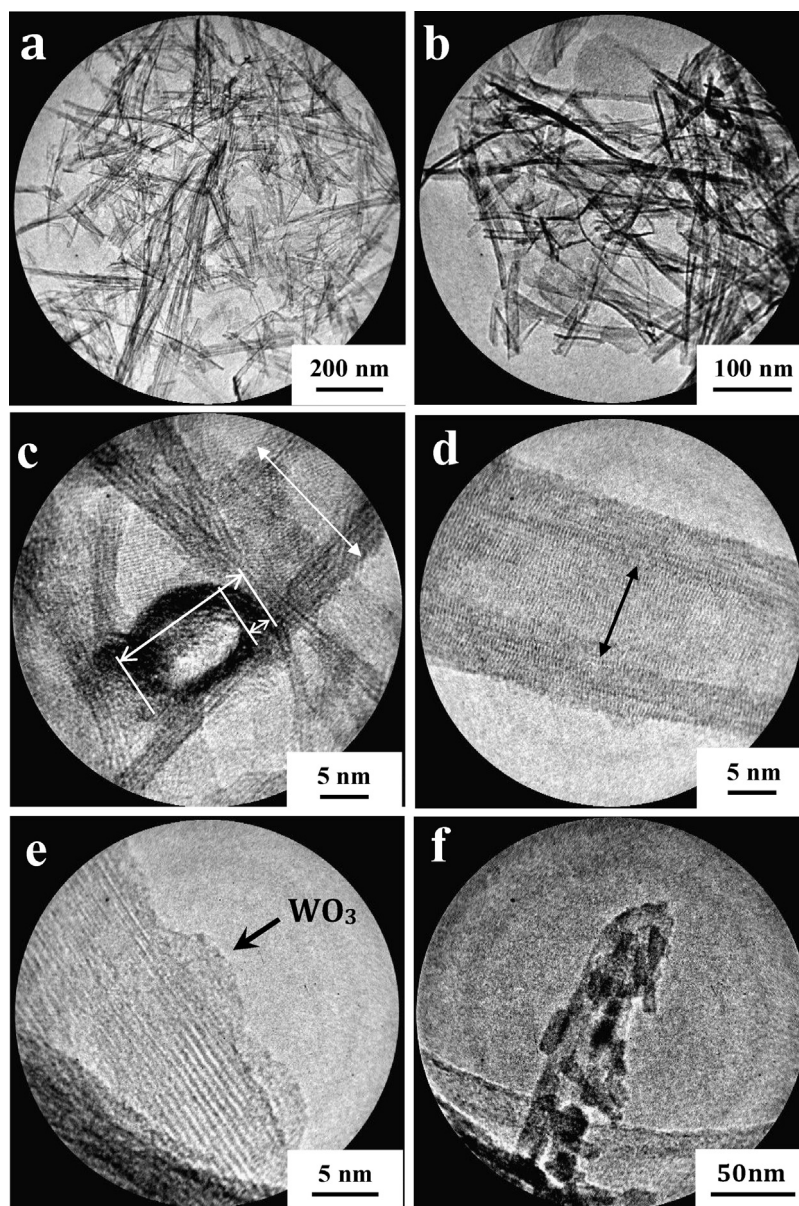**Fig. 2.** (a and b) TEM images of the as-synthesized raw Na-titanate (TiNT-Na) nanosheets.

Fig. 3. TEM images of (a) the dried TiNT-H, (b–e) the TiNT-WO$_3$ 4% calcined at 380 °C and (f) the TiNTs calcined at 380 °C with no prior impregnation with tungsten salt, evidencing the progressive degradation of the tubular morphology with the appearance of nanoparticles extracted from the nanotubes.

the thermal treatment, as proposed in the mechanism reported by Zhang et al. [49]. Although peaks are broadened, it matched the pattern for TiO$_2$ (B), taking however into account that, the presence of TiO$_2$ anatase cannot be excluded. Considering that, the nanotube materials were here still labeled as TiNT-WO$_3$ samples.

Diffraction peaks assigned to monoclinic WO$_3$ were only observed for the TiNT-WO$_3$ sample loaded with 8 wt.% WO$_3$ due to the XRD detection sensitivity and/or to the cristallinity or the good dispersion of the tungsten species on the nanotubes.

TEM images (Fig. 3), as well as SEM analysis (Fig. 4), revealed that the calcination at 380 °C of the tungsten salt-impregnated TiNTs did not alter the nanotubular morphology, with a length of few hundred of nm, no granular morphologies being observed. Open-end nanotubes were observed with a wall thickness of about 5 nm (Fig. 3b–e). The decoration of TiNTs with nano-islands of WO$_3$ particles was observed in Fig. 3f, whereas the presence of tungsten in the whole sample was confirmed by EDS analysis (Fig. 4). SEM images evidenced that calcined TiNT-WO$_3$ 4% were highly agglomerated into micron-size fibrous clusters. According to literature,

this agglomeration phenomenon is more marked in the case of short nanotubes because of their highest surface energy. Agglomeration/aggregation has been showed to remain a crucial problem especially for depositing and immobilizing these structures onto a substrate [50]. The calcination of the dried TiNT-H at 380 °C without any prior impregnation of the paratungstate salt (TiNT-380) led to the partial destruction of the tubular morphology, which turned continuously into TiO$_2$ nanoparticles extracted from the nanotubes (Fig. 3f), even if the overall macroscopic tubular morphology was maintained (not shown here). The presence of tungsten dispersed at the surface stabilized thus the TiNT tubular morphology during the temperature treatment and increased their thermal stability.

The nitrogen adsorption/desorption hysteresis isotherms of the TiNT-H, TiNT-WO$_3$ 4% and TiNT-380 samples are shown in Fig. 5A and corresponded to mainly mesoporous materials according to the well-admitted classification. The dried TiNT-H material displayed a high specific surface area of 412 m^2/g, decreasing down to 280 and 274 m^2/g for the TiNT-380 and TiNT-WO$_3$ 4% samples respectively,
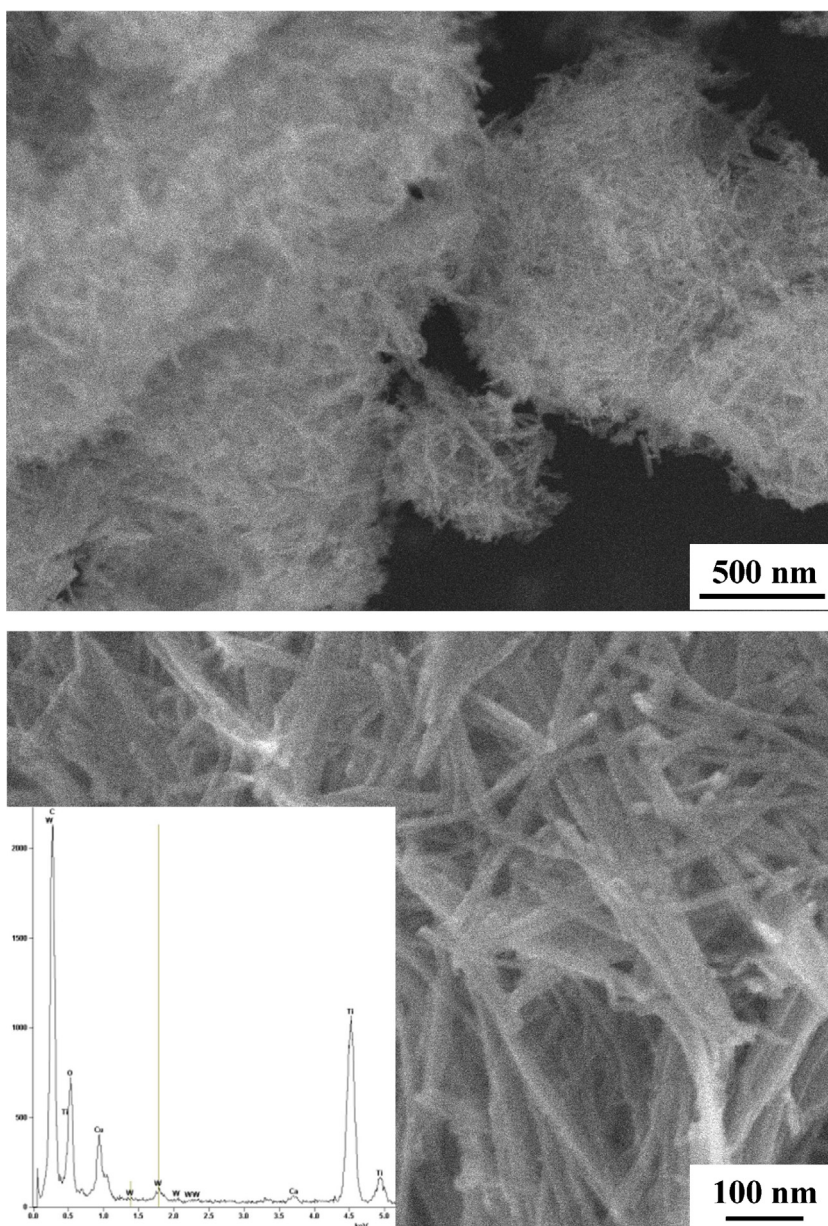
Fig. 4. SEM images and EDS spectra of the TiNT-WO$_3$ 4 wt.% photocatalyst after calcination at 380 °C.

both remaining however largely higher than that of the TiO$_2$ P25 precursor (50 m^2/g). The TiNT-based materials have no microporosity, with a specific surface area resulting mainly from both external and internal geometrical surfaces exposed by the nanotubes. The inset figure shows the monomodal and mesoporous pore size distribution of the nanotubes, in good agreement with the internal diameter of the nanotubes derived from the microscopy measurements, the internal channels of the nanotubes being seen as high aspect ratio nanopores. Thus the decrease in surface area was in line with the slight size-reduction of the internal and external diameters of the nanotubes during the thermal treatment. This shift to lower pore sizes of the monomodal pore size distribution was also qualitatively in agreement with the decrease in the channel diameter.

UV–vis absorption spectra shown in Fig. 5B evidenced the shift toward the visible light range of the spectrum for the TiNT-WO$_3$ 4% material compared to the reference TiO$_2$ P25 or to the TiNT-H, with the enlargement of the absorption tail up to about 500 nm.

3.1.2. XPS investigation

Surface characterization has been performed by XPS for analyzing the elements at the catalyst surface as well as the chemical environment of titanium, oxygen and tungsten atoms.

The titanium Ti 2p region of XPS spectra recorded on TiNT-H, TiNT-380 and fresh TiNT-WO$_3$ 4% samples is shown in Fig. 6. A single contribution was observed for both TiNT-H and TiNT-380 materials, with the doublet related to Ti 2p$^{3/2}$–Ti 2p$^{1/2}$ spin-orbit components of Ti^{4+} (Ti-O) surface species, at 459.3 and 465 eV, and 458.1 and 463.8 eV, respectively, according to literature [51]. This shift is due to a different chemical environment of Ti^{4+}, certainly resulting from the calcination step. On the TiNT-WO$_3$ 4% spectra, beside the main contribution corresponding to Ti^{4+} surface species at 458.7 and 464.4 eV, the appearance of a slight asymmetry with a peak shoulder around 459.8 eV was attributed to a supplementary contribution accounting for 14% of the total signal and assigned to surface Ti-O-W bonds, associated to Ti$_x$W$_y$O$_z$ tungsten titanate surface species. No signal associated to Ti^{3+} reduced species has been detected.
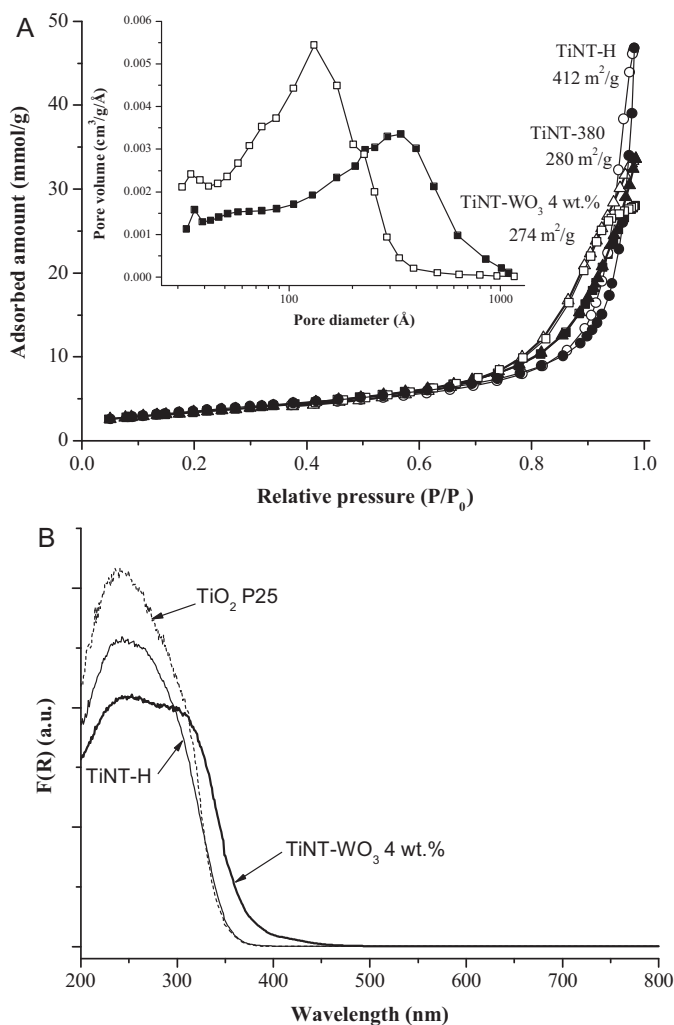
Fig. 5. (A) N_2 adsorption–desorption isotherms of (●,○) the dried TiNT-H, (■,□) the TiNT-WO$_3$ 4 wt.% calcined at 380 °C and (▲,△) the TiNT-380 calcined at 380 °C. Inset: Pore size distribution of (■ dried TiNT-H and (□) TiNT-WO$_3$ 4 wt.% calcined at 380 °C. (B) UV–vis light absorption properties of TiNT-WO$_3$ 4 wt.%, TiNT-H and TiO$_2$ P25.

Fig. 6. Ti 2p XPS spectra of (a) TiNT-H, (b) TiNT-380 as well as (c) fresh TiNT-WO$_3$ 4%, (d) TiNT-WO$_3$ 4% after test and (e) TiNT-WO$_3$ 4% after test and regeneration.

The oxygen O 1s region of the TiNT-WO$_3$ 4% spectra taken as example revealed three major contributions at 529.8, 530.7 and 531.8 eV (Fig. 7). The first contribution at 529.8 eV is due to oxygen bound to titania Ti^{4+} (O-Ti) (60%). The second contribution around 530.7 eV corresponds to surface O-W species (28%), while the last one at 531.8 eV is attributed to surface hydroxyl groups (O-H) (12%), also reported elsewhere [18].

The region of the tungsten W *4f* spectra for the TiNT-WO$_3$ 4% material, revealed a more complex multi-contribution pattern (Fig. 8). The major contribution corresponds to the W 4f$_{7/2}$–W 4f$_{5/2}$ orbital doublet of W^{6+} (W-O) (59%) at 35.6 and 37.9 eV. Beside the contribution due to titanium Ti^{4+} 3p (O-Ti) (21%) at 36.7 eV, a second W 4f$_{7/2}$–W 4f$_{5/2}$ doublet with a relative intensity of 20% has been detected at higher energies, unusual for tungsten, attributed to new surface species. Generally, for chemical species such as titanium or tungsten, a shift to higher binding energies is characteristic of a higher oxidation state or, more generally, of an electron deficiency induced by the chemical environment of the element. In our case, this new high energy contribution was attributed to W-O-Ti surface bonds associated to Ti$_x$W$_y$O$_z$ surface species, also in agreement with the Ti-W contribution detected in the Ti 2p spectrum. This species could not be identified on the O 1s spectrum, being
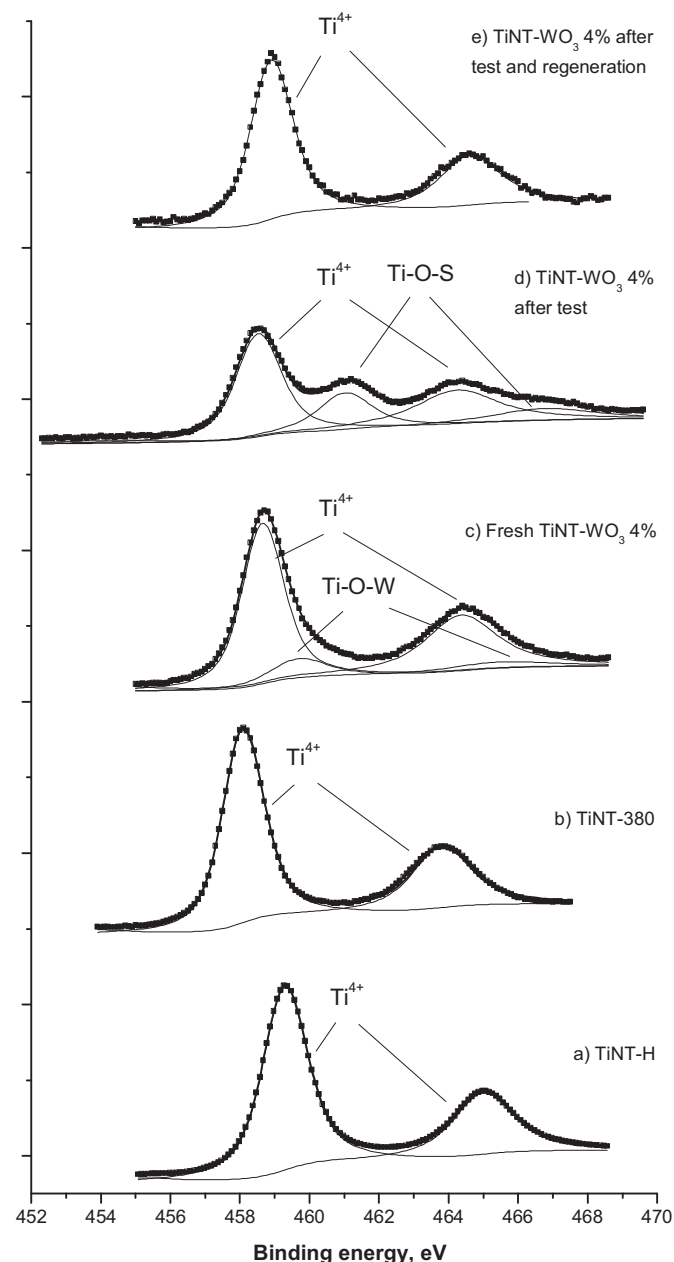
certainly embedded in the intense signal envelope formed by the three oxygen contributions, and especially by that of bonded-oxygen in WO$_3$. Thus, considering also the larger cross sections, *i.e.* greater sensitivity, of W 4f$_{7/2}$ and W 4f$_{5/2}$ orbitals, the presence of a W$_x$Ti$_y$O$_z$ species is mostly visible in the W 4f spectrum. We assume that this phase would be located at the interface between the nanotubes and the WO$_3$ phase, by resulting from an intimate contact between the nanotubes and the WO$_3$ precursor during the calcination step.

Fig. 9 shows the gradual increase of the W/O surface atomic ratio with the WO$_3$ weight content in the TiNT-WO$_3$ samples. However, this increase was not linear in the studied content range, so that a non-uniform deposition of tungstate species was assumed, as also noted by Di Gregorio et al. for the structure of tungsten oxide supported on ZrO$_2$ [52].
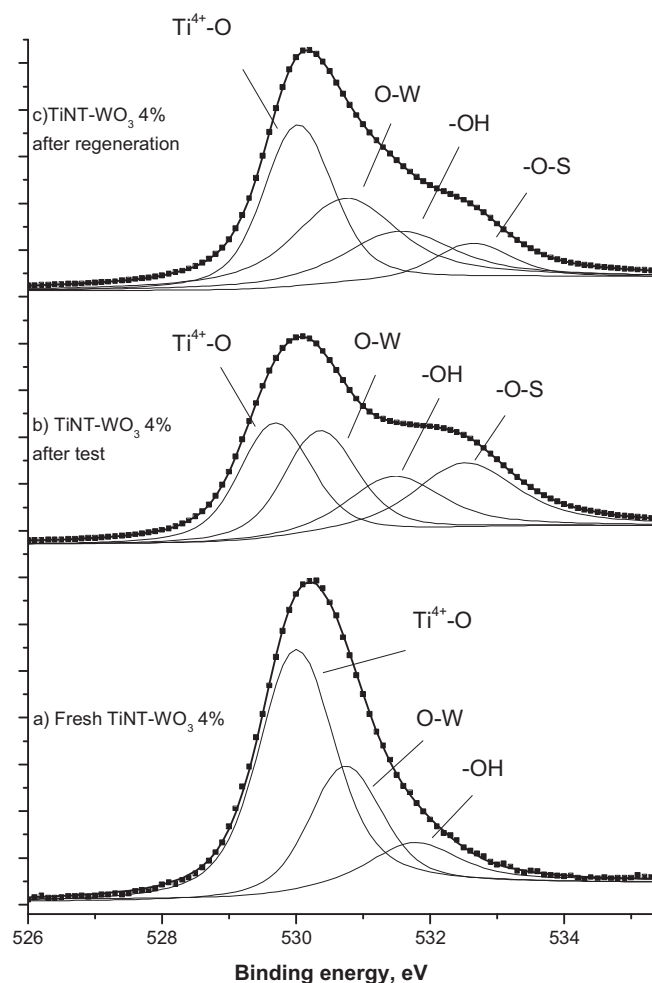
Fig. 7. O 1s XPS spectra of (a) fresh TiNT-WO₃ 4% sample showing three contributions attributed to O-Ti (529.8 eV), O-W (530.7 eV) and to –OH hydroxyl groups (531.8 eV); (b) TiNT-WO₃ 4% after test and (c) TiNT-WO₃ 4% after test and regeneration, evidencing the additional contribution attributed to O-S (532.5 eV).

Fig. 8. W 4f XPS spectra of (a) fresh TiNT-WO₃ 4% showing three contributions attributed to W-O (35.6–37.9 eV), to the Ti 3p peak (36.7 eV) and to W-O-Ti (39.7–41.9 eV); (b) TiNT-WO₃ 4% after test evidencing the additional doublet contribution attributed to W-O-S bonds (39.1–41.2 eV); and (c) TiNT-WO₃ 4% c.

3.2. Photocatalytic activity

Fig. 10 shows the influence of the WO₃ loading on the *on-stream* DES degradation obtained on TiNT-WO₃ photocatalysts under solar illumination for an inlet DES concentration of 350 ppmv, and compared to those shown by TiNT-H and TiNT-380 unmodified samples. First, total elimination of DES could be achieved on both unmodified catalysts, although further deactivation phenomenon was more pronounced on the uncalcined material. One could clearly see the important role played by WO₃ on the photocatalytic activity, with an optimal content of 4 wt.%. The TiNT-WO₃ 4% composite photocatalyst displayed a remarkable activity with a total DES abatement for about 150 min before deactivating *on-stream* to maintain a DES conversion of 70% after 360 min of test. By contrast, adding 2 wt.% and 8 wt.% of WO₃ strongly inhibited the photocatalytic reaction when compared to the WO₃-free nanotubes, considering both initial and stabilized activities, leading to a strong deactivation of the photocatalysts.

Such an influence of the WO₃ content was already reported by Li et al. in the liquid phase degradation of methylene blue under visible light irradiation over sol–gel WO₃/TiO₂ photocatalysts [29]. The authors indicated that depending on the WO₃ content, either negative or positive effects were observed. They proposed that the negative influence could result from the appearance of charge recombination centers, and by contrast, that the positive influence
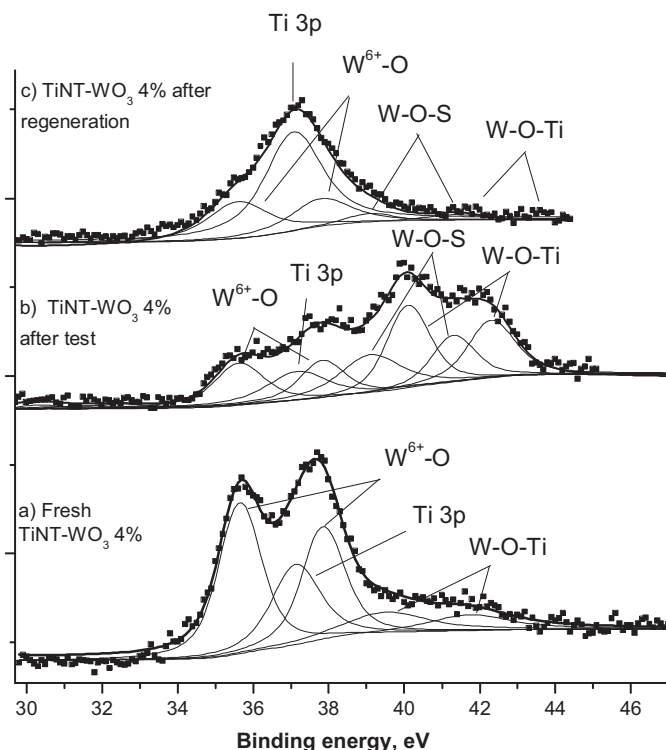
could be explained by a limitation of the photogenerated charge recombination induced by the modification. They proposed the formation of a $W_xTi_{1-x}O_2$ solid solution, leading to the emergence of intermediate energy levels depending on the tungsten content.

The TiNT-WO₃ 4% composite material was thus selected for studying the time on stream evolution of the gaseous reaction intermediates formed during the DES degradation, as well as the influence of the DES concentration and of the relative humidity (RH) on the photocatalytic activity.

Fig. 11 evidences that the DES elimination was first accompanied by the temporary formation of small amounts of diethylsulfone, followed by the continuous production of diethyldisulfide, which was
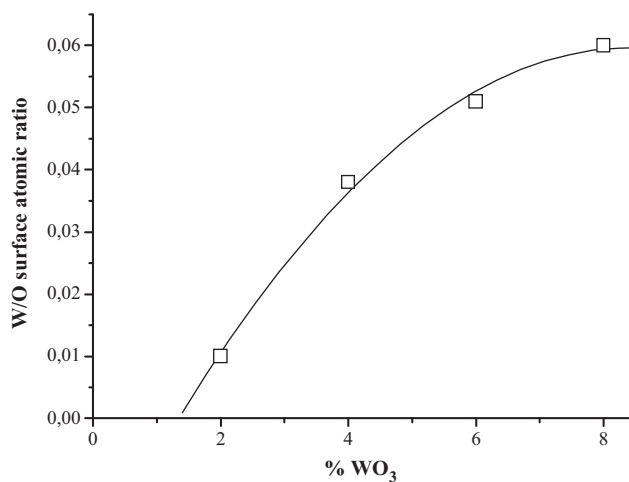

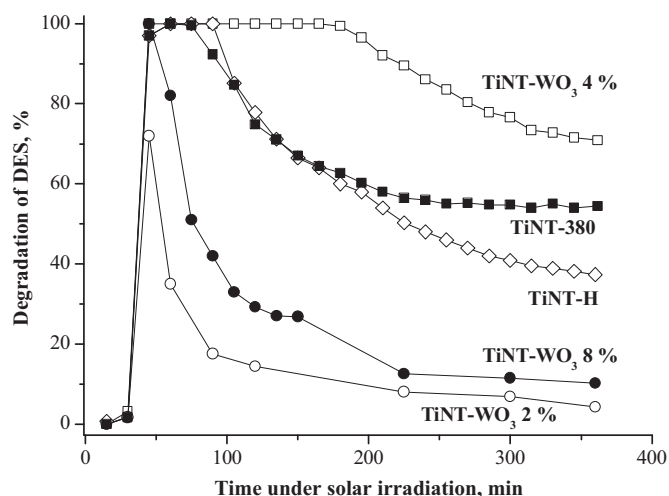**Fig. 9.** W/O surface atomic ratio for the TiNT-WO₃ nanotubes loaded with 2, 4, 6 and 8 wt.% of tungsten oxide.

Fig. 10. Photocatalytic degradation of gas phase DES on TiNT-H, TiNT-380 and on TiNT-WO$_3$ 2%, 4% and 8% under solar illumination (350 ppmv DES, 40% RH and 50 cm^3/min total flow rate).

Fig. 12. Influence of the inlet DES concentration on the gas phase DES degradation on TiNT-WO$_3$ 4% as a function of time on stream and under solar illumination (40% RH and 50 cm^3/min total flow rate).

the main intermediate reaction product detected in the gas phase. It must be mentioned that traces (close to the detection limit) of diethylsulfoxide and 3(ethylthio)propanal have also been detected.

Fig. 12 shows the evolution of the DES removal as a function of time under solar illumination for DES inlet concentrations within the 100–1000 ppmv range. Clear differences in terms of DES degradation efficiency were observed: at 100 ppmv, the degradation was complete for 9 h under continuous DES flow, whereas the photocatalyst was able to maintain such a level for 2.5 h at 350 ppmv and for few minutes at 1000 ppmv. It could also be observed that the deactivation rate as well as the stabilized degradation efficiency was strongly influenced by the DES concentration.

Fig. 13 shows the influence of the relative humidity on the DES degradation efficiency shown by the TiNT-WO$_3$ 4% photocatalyst, studied at a 100 ppmv DES inlet concentration, for which it exhibited the higher performances with only a negligible deactivation at 40% RH, so that the high activity at that concentration allows to better assess the effects brought by humidity changes. Two on-stream behaviors were observed. In dry conditions, gradual and continuous deactivation occurred after 200 min of total DES degradation,
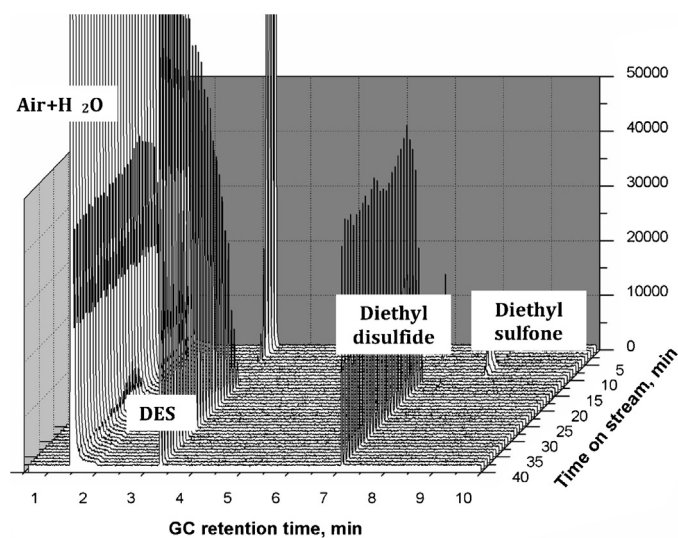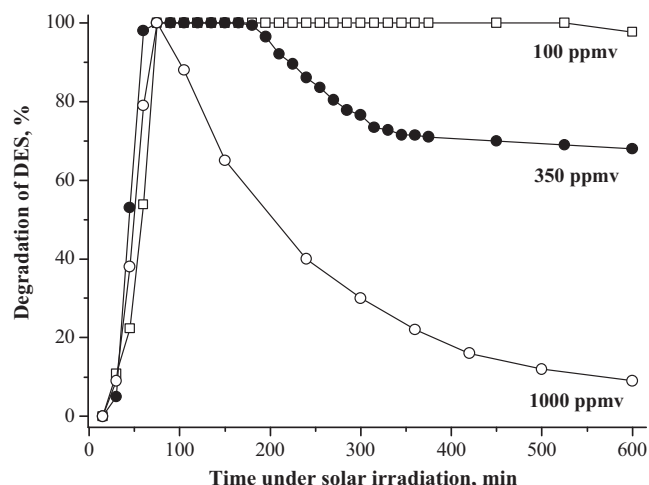
whereas by contrast, in the presence of humidity and almost independently of the humidity ratio, complete DES degradation was maintained on stream for 9 h before a very slight deactivation of few percents was recorded. However, we can suppose that increasing the relative humidity ratio above 80% would lead to a decrease in the photocatalytic activity, certainly due to adsorption competition between water and reactant molecules, as already mentioned in the literature [53]. Another hypothesis suggests the formation at very high humidity ratios of a thin water film on the catalyst surface which could dissolve organic molecules [54], so that it is also conceivable that the dissolution of the organic reactant is rate-limiting.

3.3. After test characterizations

The after test characterizations were focused on the TiNT-WO$_3$ 4% photocatalyst, after the *on-stream* photocatalytic degradation of 350 ppmv of DES at 40% RH for 10 h under artificial solar light.

3.3.1. FTIR analysis

FTIR spectra of both fresh and used TiNT-WO$_3$-4% photocatalysts are shown in Fig. 14. On the fresh photocatalyst, the massive absorption in the 3000–3500 cm^{-1} range and the low

Fig. 11. 3D chromatography showing the evolution of DES and gaseous products or intermediates during the on stream reaction on the TiNT-WO$_3$ 4% photocatalyst (350 ppmv DES, 40% RH and 50 cm^3/min total flow rate).
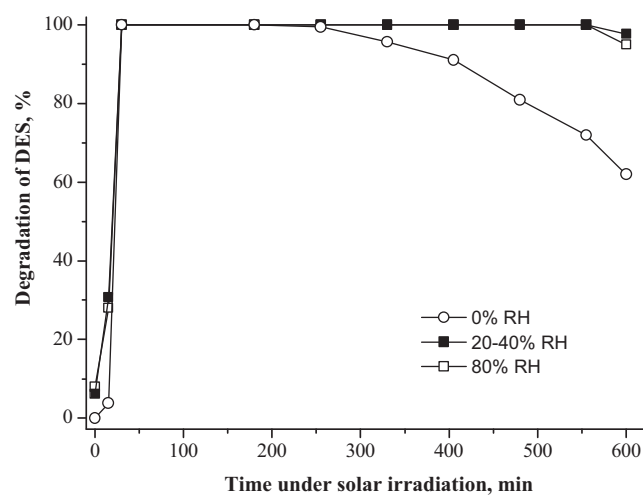

Fig. 13. Influence of the relative humidity at an inlet DES concentration of 100 ppmv on the gas phase DES degradation on TiNT-WO$_3$ 4% as a function of time on stream and under solar illumination (40% RH and 50 cm^3/min total flow rate).
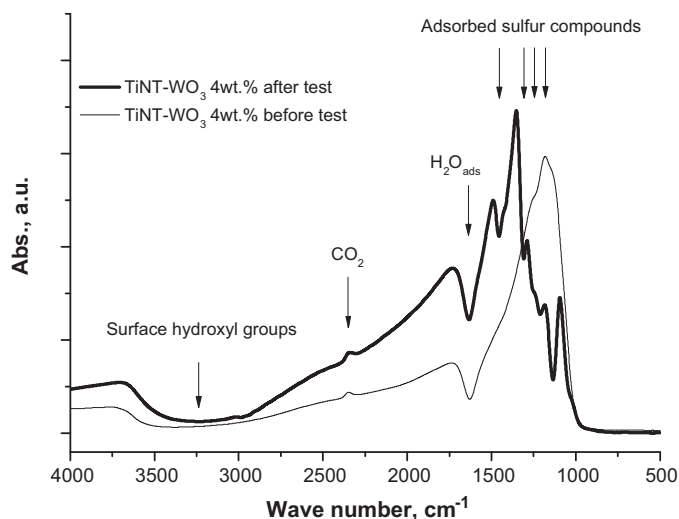
Fig. 14. Comparison of FTIR spectra of both fresh and used TiNT-WO₃ 4% photocatalyst (350 ppmv DES, 40% RH and 50 cm³/min total flow rate).

Fig. 16. Comparison of TGA weight losses of both fresh and used TiNT-WO₃ 4% photocatalyst after test (350 ppmv DES, 40% RH and 50 cm³/min total flow rate). Both SO_2 and CO_2 MS signals obtained during TPO analysis of the used TiNT-WO₃ 4% photocatalyst after test are reported.

intensity vibration band at $2350\,cm^{-1}$ were assigned to surface hydroxyl groups and adsorbed carbon dioxide, respectively, whereas the characteristic band of adsorbed water was observed at $1630\,cm^{-1}$. After test, additional vibration bands were observed mainly between 1000 and $1500\,cm^{-1}$, and were attributed to the adsorption of organic reaction products (such as sulfones or sulfoxides) [55] and to sulfates [56] (Fig. 15).

3.3.2. Thermogravimetric analysis and Temperature Programmed Oxidation

Fig. 16 compares the TGA profiles for both fresh and used TiNT-WO₃ 4% catalysts. The fresh photocatalyst underwent a mass loss of almost 7%, mainly assigned to the desorption (between 100 and
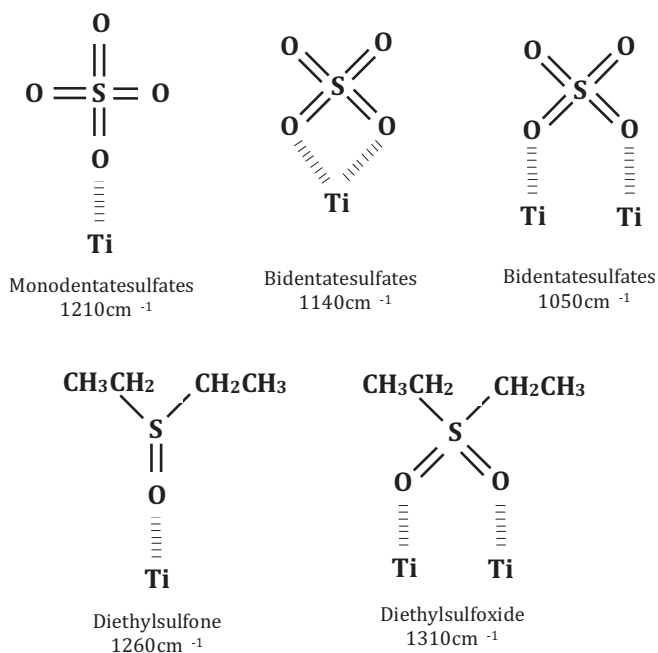
250 °C) of water molecules adsorbed on both internal and external surfaces of tubes as well as of interlayer water molecules, and to a progressive degradation of the tubular morphology above 400 °C initiated by interlayer dehydration, as classically observed. After test, the mass loss pattern differed significantly with a 18% mass loss, mainly assigned to the desorption of intermediates or reaction products responsible for the catalyst deactivation. Coupled to SO_2 and CO_2 TPO profiles, the TGA pattern evidenced five distinct mass losses, that could be assigned to:

 (I) the elimination of adsorbed surface water (4.5%). No release of SO_2 or CO_2 molecules was observed till 100–150 °C.
(II) the removal of interlayer water and the oxidative desorption of a first category of sulfur-containing hydrocarbon molecules with a maximum around 200 °C (7.5%). Under an oxidative atmosphere, sulfur-containing hydrocarbon molecules may desorb as CO_2 and SO_2. This could correspond to unreacted diethylsulfide.
(III) the oxidative desorption as CO_2 and SO_2 of a second group of sulfur-containing organic molecules with a maximum at about 300 °C (3%). This could correspond to diethyldisulfide or to other reaction intermediates.
(IV) the desorption of another class of organic compounds with a maximum around 400 °C due to the oxidative desorption as CO_2 of species containing only carbon and no sulfur. One should note that, like for fresh nanotubes, the thermal degradation of the tubular morphology was initiated by the interlayer dehydration with increasing the temperature, and was accompanied by the release of water (1%), even if this weight loss remained slightly hidden by the broad and more pronounced release of CO_2 and SO_2 occurring over several hundred degrees and was thus less visible than on fresh nanotubes.
 (V) the high temperature decomposition of mono- or bidentates sulfate species exclusively into SO_2, above 500 °C with a maximum at about 550–600 °C (4%).

Fig. 15. Sulfates and organic species adsorbed on the TiNT-WO₃ 4% photocatalyst after DES photocatalytic test (350 ppmv DES, 40% RH and 50 cm³/min total flow rate).
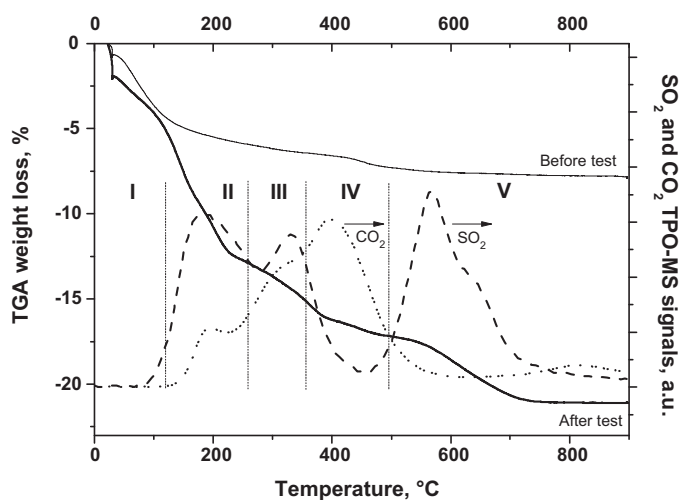
One should mention that the evidence of distinct weight loss ranges remains indicative, due to the overlap of the different contributions.
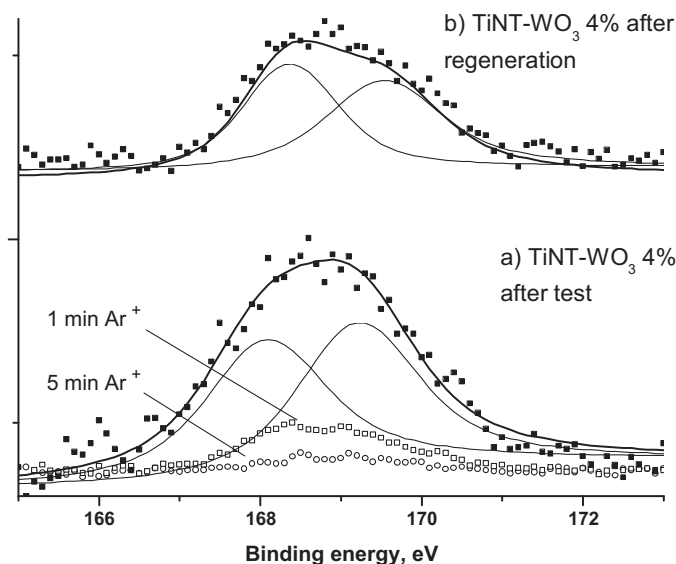
Fig. 17. Sulfur S 2p XPS spectra of a) TiNT-WO₃ 4% after photocatalytic test (350 ppmv DES, 40% RH and 50 cm³/min total flow rate) and Ar⁺ bombardment for 1 min and 5 min; and of b) TiNT-WO₃ 4% after test and regeneration.

3.3.3. XPS investigation

In parallel to the intensity decrease of the doublet corresponding to Ti⁴⁺, the Ti 2p XPS spectra of the used photocatalyst displayed the appearance of an additional higher energy doublet at 461.1 and 466.9 eV accounting for 31% of the signal and assigned to a Ti-O-S binding (Fig. 6). It was very difficult to evidence the Ti-O-W contribution, that was already relatively difficult to observe on the spectra of the fresh material, so that test we cannot discuss whether the disappearance or the diminution of this contribution after test.

The S 2p XPS spectra recorded on the used photocatalyst shown in Fig. 17 exhibited two contributions attributed to the doublet related to the S $2p_{3/2}$–S $2p_{1/2}$ spin–orbit components in a high oxidation state, and assigned to surface S⁶⁺ sulfate species [57]. The presence of surface polysulfate species which could result from a partial and local polymerization of sulfates, or of sulfates with different coordination modes to Ti⁴⁺, could explain the unusual $2p_{3/2}/2p_{1/2}$ surface ratio observed. Even if some organic sulfur-containing reaction intermediates probably remained adsorbed at the catalyst surface after test, they should desorb during XPS analysis or are not observed due to the XPS detection limit. Surface sulfates as well as some adsorbed partially oxidized reaction intermediates, are reported to cause the deactivation of photocatalysts during the degradation of sulfur-containing organic molecules [5,9,58–61], whereas only sulfates are concerned in the degradation of H₂S [62,63]. The decrease of the S/Ti surface atomic ratio down to zero after 5 min of argon ion bombardment confirmed the presence of sulfur species at the material surface (Table 1).

After test, the O 1s XPS spectra shown in Fig. 7 evidenced a new contribution at 532.5 eV assigned to surface O-S bonds, with a relative content of 25%, that may be associated with surface sulfates,

more probably than with the detection of adsorbed organic sulfur for the above-mentioned reason. This was accompanied with a large decrease in the O-Ti⁴⁺ contribution (28%), whereas that of the O-H surface species was not much affected, so that it was proposed that O-Ti (Ti⁴⁺) sites would act as the main active sites in the DES photocatalytic oxidation reaction on TiNT-WO₃ materials. This was also put forward in the photocatalytic degradation of H₂S, that was proposed to mainly take place on TiO₂ through the molecular adsorption of H₂S on Ti⁴⁺ surface sites *via* the central sulfur atom of H₂S [63]. It should be noted that a slight shift toward lower energy was observed for oxygen contributions, as already reported for sulfated titania systems, and resulting from a possible electron transfer to surface sulfates [64].

The XPS spectra of the W 4f energy zone displayed an additional doublet for W $4f_{7/2}$ and W $4f_{5/2}$ orbitals at 39.1 and 41.2 eV, assigned to W-O-S surface bonds with 28% of relative content (Fig. 8). A decrease in both W⁶⁺ (W-O) and Ti⁴⁺3p (Ti-O) contributions was observed, down to 23% and 11% in relative content, respectively, in agreement with the decrease in the O-Ti contribution recorded on both Ti 2p and O 1s spectra.

The parallel decrease of W-O and Ti-O contributions were assumed to correspond mostly to a partial coverage of Ti⁴⁺ (O-Ti) surface sites and of W⁶⁺ (W-O) tungsten oxide surface sites, as confirmed by the appearance of both Ti-O-S (Fig. 6) and W-O-S (Fig. 8) bond contributions, respectively.

3.3.3.1. Comparison before/after regeneration.
A thermal regeneration of the catalyst under humid air at 90 °C led to the desorption of organic compounds reversibly adsorbed on the catalyst surface, DES as well as intermediates like diethyldisulfide or diethylsulfone being detected by GC-MS in the outlet flow during the heat treatment. Ti *2p* XPS spectrum of the catalyst after regeneration evidenced only a single contribution assigned to Ti⁴⁺, so that titanium-bonded sulfur compounds (within the detection limit) desorbed or were decomposed during the regeneration (Fig. 6). After thermal regeneration, the O-S bond contribution in the O 1s spectrum and the S 2p orbital doublet assigned to surface sulfate species were still observed on the catalyst, as shown in Figs. 7 and 17, respectively. The contribution attributed to W-O-S bonds in the W $4f_{7/2}$ and W $4f_{5/2}$ orbital energy zone decreased without any complete disappearance, as well as of that assigned to the $Ti_xW_yO_z$ species, although the intensity was close to the detection and deconvolution limit, representing less than 5% of the total area (Fig. 8). In parallel, a significant increase in the Ti 3p contribution was recorded.

Surface modification related to the presence of sulfur species after thermal reconditioning were quantified by the decrease down to zero of the S/Ti surface atomic ratio, while the persistence of the sulfur signal attributed mainly to sulfates resulted only to a partial decrease in the S/W surface atomic ratio down to 0.021 (Table 1). The persistence of sulfur compounds on the surface, but not in interaction with titanium, evidenced that the thermal regeneration led to desorb or degrade the main organic sulfur species adsorbed on Ti⁴⁺ sites, whereas W⁶⁺ sites (and probably also the $W_xTi_yO_z$ phase) were still in close interaction with inorganic sulfur (sulfates) and also probably with some adsorbed organic sulfur in low content.

3.4. Discussion

3.4.1. Reaction mechanism pathways and role of surface sites
From the evolution of DES and gas phase reaction products shown in Fig. 11, a reaction pathway can be proposed (Fig. 18), considering as first steps either the direct oxidation of DES by the photogenerated holes (h⁺) leading to diethylsulfinium radicals [1] or the oxidation through hydroxyl radicals [2]. In this last case, hydroxyl radicals can oxidize the sulfur atom [1–2] or the carbon

Table 1
S/Ti and S/W surface atomic ratios derived from XPS surface analysis on the fresh, the tested and the regenerated TiNT-WO₃ 4 wt.% photocatalyst. Ar⁺ ion bombardments have been performed for 1 min and 5 min on the used photocatalyst.

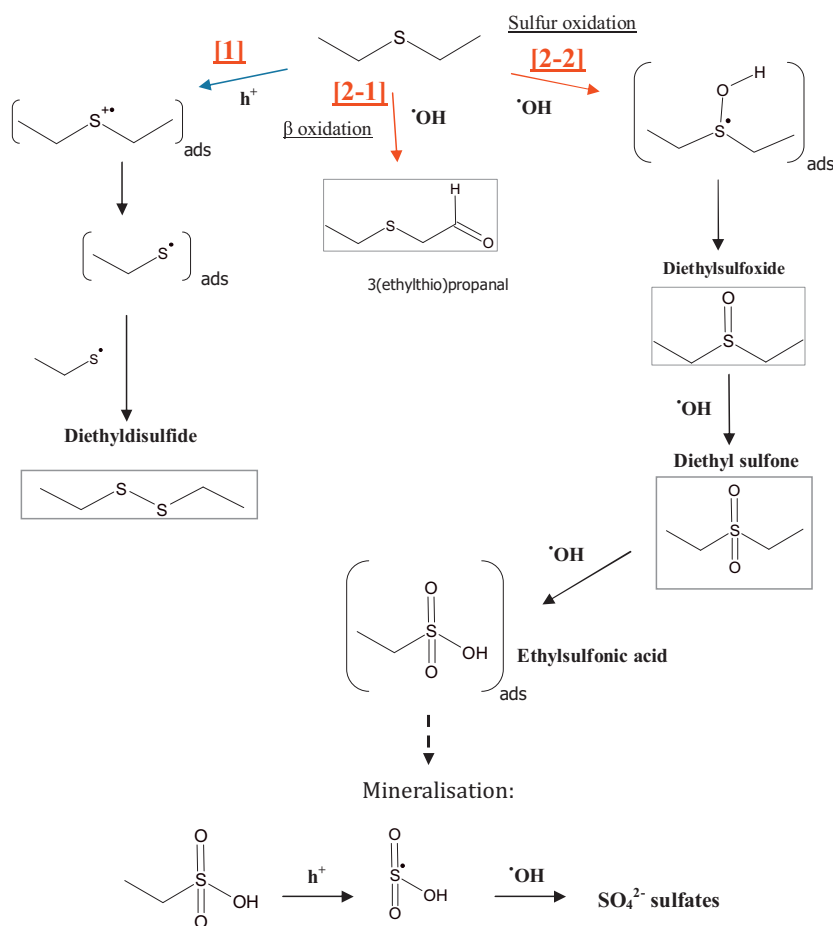| TiNT-WO₃ 4 wt.%	S/Ti	S/W
Fresh	0	0
After test	0.109	0.04
After 1 min Ar⁺	0.006	
After 5 min Ar⁺	*ca.* 0	
After regeneration	0	0.021

Fig. 18. Reaction pathways for gas phase DES photooxidation on TiNT-WO$_3$ 4%.

in β-position [2]. Step [1] mainly occurs through adsorption of DES on Ti^{4+} sites, and the progressive elimination of DES in favor of diethyldisulfide (main reaction product) is proposed to result from the dimerization of the ethanethyl radical, itself issued from C-S cleavage in the diethylsulfide radical cation. The presence of diethyldisulfide at high concentration also means that it remains weakly adsorbed on the surface, and probably could not be subsequently and ultimately oxidized into sulfates. By contrast, steps [2] are initiated by the adsorption of DES on hydroxyl surface species. Diethylsulfoxide would result from the direct oxidation of the sulfur atom of DES with hydroxyl radicals [2]. However, it was only detected at traces level, meaning that this intermediate was either rapidly oxidized into diethylsulfone or strongly adsorbed on the surface. However, the initial and temporary presence of diethylsulfone also suggests that it undergoes further oxidation step in the adsorbed phase, leading to ultimate oxidation into sulfate species. It was also mentioned previously that 3(ethylthio)propanal was detected in the gas phase, close to detection limit. It resulted from the direct oxidation of the β-carbon in DES by hydroxyl radicals. Nevertheless, no products issued from the oxidation of the carbon in α-position have been detected.

There is a correlation between the DES degradation activity and the photocatalyst surface composition. It is proved that the surface of TiO$_2$ has at least two kinds of adsorption sites, Ti^{4+} cations and hydroxyl groups [5]. However, the DES is more likely to be adsorbed on Ti^{4+} sites through the sulfur atoms, before to adsorb further on hydroxyl groups after the saturation of Ti^{4+} occurred. Taking into account that the DES has an ionization potential among the lowest of all sulfur compounds involved, *i.e.* DES will be more easily

ionized by the photogenerated holes than sulfur-containing reaction intermediates issued from the DES degradation, active holes will first react in priority with DES on Ti^{4+} surface sites. Thus, either sulfur-containing partially oxidized reaction intermediates remained preferentially adsorbed on Ti^{4+} sites, – with a lower reactivity than DES molecules –, leading therefore to reduce the number of sites available for further adsorption of DES, or, like diethylsulfone molecules, they are assumed to react further on hydroxyl groups. The gradual activity decline with time on stream from total degradation to stabilization would thus result from: (i) the progressive deposition of surface sulfates as ultimately oxidized product and blocking the active sites of the photocatalyst, and (ii) this competition on Ti^{4+} sites and hydroxyl groups at the photocatalyst surface, between both adsorption and reactivity of DES and those of reaction intermediates. Thus, in addition to the visible-light absorption rate, the specific surface area or the recombination rate of the photocatalyst, those TiO$_2$ surface site phenomena would be responsible in part for the steady-state or the long term activity of the catalyst.

3.4.2. Role of surface acidity

The high adsorption capacity of the TiNT-WO$_3$ 4% photocatalyst toward DES and sulfur-containing reaction intermediates could also explain its significant activity, as a result from a high specific surface area as well as from an increased number of surface acid sites, which may be formed through the addition of WO$_3$. Indeed, H-TiNT displayed an IEP of 5.3, in agreement with the literature [11,12], indicating the presence of a slight acidity due to the chemical composition of the TiNT surface, when compared to the

quasi-neutral surface of TiO$_2$ P25 (Evonik), for which an IEP of 6.8 was measured. By contrast, the TiNT-WO$_3$ 4% photocatalyst exhibited a more acidic surface, with an IEP of 3.4. It should be noted that WO$_3$ is often used in heterogeneous catalysis for acidifying the surface of oxide catalysts [65], the IEP of the bare oxide being evaluated between 0.2 and 0.5 leading the oxide to be seen as an acidic oxide [66]. The main active sites exposed by TiO$_2$, *i.e.* Ti^{4+} and Ti-OH sites, display Lewis and Brønsted acidity, respectively. Yates et al. have already shown that 2-chloroethyl ethyl sulfide molecules could bind to Ti-OH groups *via* sulfur atoms (and chlorine) [67,68]. We showed that the ultimate oxidation products, that is to say sulfates, accumulate mainly on W^{6+} sites of WO$_3$ oxide and perhaps on Ti$_x$W$_y$O$_z$ sites certainly due the acidity developed. We assume that these sulfates formed by the oxidation of reaction intermediates issued from DES degradation, initially adsorbed on Ti-OH active sites, migrate to more acidic surface sites such as W^{6+} or Ti$_x$W$_y$O$_z$ for which they have a stronger affinity, leaving Ti-OH sites free for further adsorption.

3.4.3. Morphology and TiO$_2$ - WO$_3$ coupling

The semiconductor morphology can lead to interesting features, such as light absorption or interfacial transfer of charges. Here, the nano-tubular morphology associated in optimal conditions and in optimal amount to WO$_3$ is certainly the key to the interesting photocatalytic behavior of the materials.

On TiNT-WO$_3$ composite photocatalysts, the solar light illumination led to a simultaneous activation of both WO$_3$ and TiO$_2$ phases, in both visible and UVA spectral ranges for WO$_3$, and only in the UV-A light range for the nanotubes, according to their respective band gap values. In addition, the suitable relative location of both WO$_3$ and titanate nanotube energy band levels allowed the migration of the photogenerated electrons from the nanotube conduction band to that of WO$_3$, and of the holes from the WO$_3$ valence band to that of the nanotubes. The vectorial charge transfer would limit and slow down the phenomena of photogenerated charge recombination. The solid-solid interface between TiNT and WO$_3$ is a key structural feature that allows absorption of part of the visible light and facilitates the charge photogenerated separation and prevents recombination, thereby increasing the photocatalytic efficiency. Schwab and Pietsch have been the first in 30's to discuss the existence of active sites at the interface of two solid phases and have postulated that an increase in catalytic activity was due to the interfaces between the crystals [69]. The work of Pichat et al. showed both existence and direction of electron transfer between CdS and TiO$_2$ particles, which was also depending on the preparation conditions [70]. The interaction between phases in composite materials can result in structurally different sites at the interface, and the existence of a non-stoichiometric phase at the solid-solid interface has already been raised for TiO$_2$/metal [71] and TiO$_2$/semiconductor nanocomposites [70]. The solid-solid interface between the titanate nanotubes and WO$_3$, materialized by W$_x$Ti$_y$O$_z$, lies in the formation of a third phase [28]. As mentioned above, this intermediate structure would facilitate the transfer of photogenerated charges and absorb some wavelengths of the visible spectral range, leading thus to enhance the overall photocatalytic efficiency.

4. Conclusion

In this study, we have shown that photocatalytic materials made of high surface area WO$_3$-modified titania nanotubes have great potential in the gas phase for the continuous solar light elimination of DES, taken as simulant of the live yperite blister CWA, *i.e.* mustard gas. They were prepared by hydrothermal treatment of TiO$_2$ powder, with tungstate salt impregnation on the as-synthesized titanate nanotubes prior to the final calcination step at 380 °C.

DES can adsorb and react in priority on Ti^{4+} and further on Ti-OH surface sites, leading to propose different reaction pathways to explain the sulfur-containing partially oxidized reaction intermediates observed on-stream. Competition should take place between DES and reaction intermediates in terms of adsorption and reactivity on both kinds of surface sites. Together with the deposition of surface sulfate species, this surface competition was responsible for the on-stream deactivation of the photocatalysts toward DES elimination. The modification with 4 wt.% of WO$_3$ significantly enhanced the photocatalytic activity in terms of DES removal efficiency and of resistance to sulfate deactivation. The formation of WO$_3$-TiO$_2$ heterojunctions and of Ti$_x$W$_y$O$_z$ domains assumed to be located at the TiO$_2$-WO$_3$ interface allowed both TiO$_2$ photosensibilisation in the beginning of the visible light range as well as beneficial charge transfer and separation. Also, WO$_3$ and Ti$_x$W$_y$O$_z$ domains exhibiting higher surface acidities than TiO$_2$ were also proposed to limit the deactivation phenomena, by leaving the Ti-OH active sites free of poisoning sulfates for further photooxidation of DES and of partially oxidized reaction intermediates.

Appendix A. Supplementary data

Supplementary data associated with this article can be found, in the online version, at http://dx.doi.org/10.1016/j.apcatb.2013.02.041.

References

[1] D.F. Ollis, H. Al-Ekabi (Eds.), Photocatalytic Purification and Treatment of Water and Air, Elsevier, Amsterdam, 1993.
[2] A.V. Vorontsov, E.V. Savinov, L. Davydov, P.G. Smirniotis, Applied Catalysis B: Environmental 32 (2001) 11.
[3] A.V. Vorontsov, C. Lion, E.N. Savinov, P.G. Smirniotis, Journal of Catalysis 220 (2003) 414.
[4] K.E. O'Shea, S. Beightol, I. Garcia, M. Aguilar, D.V. Kalen, W.J. Cooper, Journal of Photochemistry and Photobiology A 107 (1997) 221.
[5] D. Kozlov, A.V. Vorontsov, P.G. Smirniotis, E.N. Savinov, Applied Catalysis B: Environmental 42 (2003) 77.
[6] M. Grandcolas, A. Louvet, N. Keller, V. Keller, Angewandte Chemie 48 (2009) 161.
[7] B. Cojocaru, V.I. Parvulescu, E. Preda, G. Epure, V. Somoghi, E. Carbonell, M. Alvaro, H. Garcia, Environmental Science and Technology 42 (2008) 4908.
[8] S. Neatu, V.I. Parvulescu, G. Epure, N. Petrea, V. Somoghi, G. Ricchiardi, S. Bordiga, A. Zecchina, Applied Catalysis B: Environmental 91 (2009) 546.
[9] C. Cantau, S. Larribau, T. Pigot, M. Simon, M.T. Maurette, S. Lacombe, Catalysis Today 122 (1–2) (2007) 27.
[10] Z.R. Tian, J.A. Voigt, J. Liu, B. McKenzie, H. Xu, Journal of the American Chemical Society 125 (2003) 12384.
[11] M. Miyauchi, H. Tokudome, Thin solid films 515 (2006) 2091.
[12] H. Tokudome, M. Miyauchi, Chemistry Letters 33 (2004) 1108.
[13] M. Zhang, Z.S. Jin, J.W. Zhang, X.Y. Guo, J.J. Yang, W. Li, X.D. Wang, Z.J. Zhang, Journal of Molecular Catalysis A: Chemical 217 (2004) 203.
[14] J.G. Yu, H.G. Yu, B. Cheng, C. Trapalis, Journal of Molecular Catalysis A: Chemical 249 (2006) 135.
[15] M.W. Xiao, L.S. Wang, X.J. Huang, Y.D. Wu, Z. Dang, Journal of Alloys and Compounds 470 (1–2) (2009) 486.
[16] C.-T. Hsieh, W.-S. Fan, W.-Y. Chen, J.Y. Lin, Separation and Purification Technology 67 (3) (2009) 312–318.
[17] M. Qamar, C.R. Yoon, H.J. Oh, N.H. Lee, K. Park, D.H. Kim, K.S. Lee, W.J. Lee, S.J. Kim, Catalysis Today 131 (1–4) (2008) 3.
[18] B.D. Yao, Y.F. Chan, X.Y. Zhang, W.F. Zhang, Z.Y. Yang, N. Wang, Applied Physics Letters 82 (2003) 281.
[19] T. Kasuga, M. Hiramatsu, A. Hoson, T. Sekino, K. Nihara, Advanced Materials 11 (1999) 1307.

[20] T. Tachikawa, S. Tojo, M. Fujitsuka, T. Sekino, T. Majima, The Journal of Physical Chemistry B: Letters 110 (2006) 14055.
[21] T. Kasuga, M. Hiramatsu, A. Hoson, T. Sekino, K. Niihara, Langmuir 14 (1998) 3160.
[22] C. Martin, I. Martin, V. Rives, L. Palmisano, M. Schiavello, Journal of Catalysis 134 (1992) 434.
[23] Y.T. Kwon, K.Y. Song, W.I. Lee, G.J. Choi, Y.R. Do, Journal of Catalysis 191 (2000) 192.
[24] C. Martin, G. Solana, V. Rives, G. Marci, L. Palmisano, A. Sclafani, Catalysis Letters 49 (1997) 235.
[25] F. Bosc, D. Edwards, N. Keller, V. Keller, A. Ayral, Thin Solid Films 495 (2006) 272.
[26] N. Keller, E. Barraud, F. Bosc, D. Edwards, V. Keller, Applied Catalysis B: Environmental 70 (2007) 423.
[27] C.-F. Lin, C.-H. Wu, Z.-N. Onn, Journal of Hazardous Materials 154 (2008) 1033.
[28] X.Z. Li, F.B. Li, C.L. Yang, W.K. Ge, Journal of Photochemistry and Photobiology A: Chemistry 141 (2–3) (2001) 209.
[29] A. Rampaul, I.P. Parkin, S.A. O'Neill, J. DeSouza, D.E. Williams, Polyhedron 22 (2003) 35.
[30] L. Cheng, X. Zhang, B. Liu, H. Wang, Y. Li, Y. Huang, Z. Du, Nanotechnology 16 (2005) 1341.
[31] Y.C. Nah, A. Ghicov, D. Kim, S. Berger, P. Schmuki, Journal of the American Chemical Society 130 (48) (2008) 16154.
[32] S. Doniach, M. Sunjic, Journal of Physics C: Solid State Physics 3 (2) (1970) 285.
[33] D.A. Shirley, Physical Review B 5 (1972) 4709.
[34] J.H. Scofield, Journal of Electron Spectroscopy and Related Phenomena 8 (1976) 129.
[35] V. Keller, P. Bernhardt, F. Garin, Journal of Catalysis 215 (2003) 129.
[36] S. Anderson, Acta Crystallographica 15 (1962) 194.
[37] H. Izawa, S. Kikkawa, M. Koizumi, Journal of Physical Chemistry 86 (1982) 5023–5026.
[38] A. Sauvet, S. Baliteau, C. Lopez, P. Fabry, Journal of Solid State Chemistry 177 (2004) 4508.
[39] D. Bavykin, J.M. Friedrich, Advanced Materials 18 (2006) 2807.
[40] Q. Chen, W. Zhou, G. Du, L.-M. Peng, Advanced Materials 14 (2002) 1208.
[41] X. Sun, Y. Li, Chemistry: A European Journal 9 (2003) 2229.
[42] G.H. Du, Q. Chen, R.C. Che, Z.Y. Yuan, L.M. Peng, Applied Physics Letters 79 (2001) 3702.
[43] R. Ma, Y. Banda, T. Sasaki, Chemical Physics Letters 380 (2003) 577.
[44] J. Yang, Z. Jin, X. Wang, W. Li, J. Zhang, S. Zhang, Z. Guo, Z. Zhang, Dalton Transactions 20 (2003) 3898.
[45] T. Beuvier, PhD Dissertation, University of Nantes, 2009.
[46] H.-L. Kuo, C.-Y. Kuo, C.-H. Liu, J.-H. Chao, C.-H. Lin, Catalysis Letters 113 (2007) 7.
[47] A.R. Armstrong, G. Armstrong, J. Canales, P. Bruce, Angewandte Chemie International Edition 43 (2004) 2286.
[48] J.G. Yu, H.G. Yu, B. Cheng, X.J. Zhao, Q.J. Zhang, Journal of Photochemistry and Photobiology A 182 (2006) 121.
[49] S. Zhang, Q. Chen, L.-M. Peng, Physical Review B 71 (2005) 014104.
[50] Y. Suzuki, B.P. Pichon, M. Grandcolas, N. Keller, V. Keller, S. Yoshikawa, Transactions of the Materials Research Society of Japan 34 (3) (2009) 545.
[51] A. Kleinhammes, G.W. Wagner, H. Kulkanu, Y. Jia, Q. Zhang, L.C. Qin, Y. Wu, Chemical Physics Letters 411 (1–3) (2005) 93.
[52] F. Di Gregorio, V. Keller, Journal of Catalysis 215 (2003) 129.
[53] A.V. Vorontsov, E.N. Kurkin, E.N. Savinov, Journal of Catalysis 186 (1999) 318.
[54] L. Cao, Z. Gao, S.L. Suib, T.N. Obee, S.O. Hay, J.D. Freihaut, Journal of Catalysis 196 (2000) 253.
[55] N. Gonzalez-Garcia, J.A. Ayllon, X. Doménech, J. Peral, Applied Catalysis B 52 (2004) 69.
[56] S. Han, G. Zhang, H. Xi, D. Xu, X. Fu, X. Wang, Catalysis Letters 122 (2008).
[57] J.F. Moulder, W.F. Stickle, P.E. Sobol, D.E. Bombon, Handbook of X-ray Photoelectron Spectroscopy, Perkin Elmer Corporation, Eden Prairie, Minesota, USA.
[58] J. Peral, X. Domenech, D.F. Ollis, Journal of Chemical Technology and Biotechnology 70 (1997) 117.
[59] N. González-Garcı́a, J.A. Ayllón, X. Doménech, J. Peral, Applied Catalysis B: Environmental 52 (1) (2004) 69.
[60] K. Demeestere, J. Dewulf, B. De Witte, H. Van Langenhove, Applied Catalysis B: Environmental 60 (2005) 93.
[61] PhD Thesis Mathieu Grandcolas, University of Strasbourg, 2009.
[62] R. Portela, M.C. Canela, B. Sánchez, F.C. Marques, A.M. Stumbo, R.F. Tessinari, J.M. Coronado, S. Suárez, Applied Catalysis B: Environmental 84 (3–4) (2008) 643.
[63] A. Alonso-Tellez, D. Robert, N. Keller, V. Keller, Applied Catalysis B: Environmental 115–116 (2012) 209.
[64] E. Barraud, F. Bosc, D. Edwards, N. Keller, V. Keller, Journal of Catalysis 235 (2005) 318.
[65] L.H. Gielgens, M.G. van Kampen, M.M. Broek, R. van Hardeveld, V.J. Ponec, Journal of Catalysis 154 (1995) 201.
[66] M. Kosmulski, Chemical Properties of Material Surfaces, Marcel Dekker, 2001.
[67] D.A. Panayotov, J.T. Yates Jr., Journal of Physical Chemistry B 107 (2003) 10560.
[68] T.L. Thompson, D.A. Panayotov, J.T. Yates Jr., Journal of Physical Chemistry B 108 (2004) 16825.
[69] E. Pietsch, A. Kotowski, G. Berend, Zeitschrift fur Physikalische Chemie 5 (1929) 1.
[70] P. Pichat, E. Borgarello, J. Disdier, J.M. Herrmann, E. Pelizzetti, N. Serpone, Journal of the Chemical Society, Faraday Transactions 184 (1988) 261.
[71] V. Subramanian, E.E. Wolf, P.V. Kamat, Langmuir 19 (2003) 469.